

Investigations of autoignition and propagation of supersonic ethylene flames stabilized by a cavity

Zhiwei Huang, Huangwei Zhang*

Department of Mechanical Engineering, National University of Singapore, 9 Engineering Drive 1, Singapore 117576, Republic of Singapore

HIGHLIGHTS

- Autoignition and propagation of supersonic ethylene flame is investigated numerically.
- The time scale and energy balance methods are developed to study flame stabilization.
- The two methods show good validity in the autoignition process of the ethylene flame.
- Premixed combustion mode is dominant during the flame autoignition process.
- Diffusion combustion mode is dominant when the flame is finally stabilized.

ARTICLE INFO

Keywords:

Supersonic combustion
Autoignition
Flame stabilization
Large eddy simulation
Ethylene flame
Strut and cavity combination

ABSTRACT

Two analysis methods for time scale and energy balance relevant to flame ignition and stabilization in cavity-stabilized flames are developed. The interaction time of hot product in the recirculation zone of the cavity with the surrounding unburned mixture and the reaction induction time of the mixture are estimated in the time scale method. The energy release from chemical reactions and the energy loss due to species exchange in the recirculation zone are included in the energy balance method. The autoignition and propagation of supersonic ethylene flames in a model supersonic combustor with a cavity is investigated first using highly resolved large eddy simulation. The evolutions of the two time scales are then calculated in the ignition process of the supersonic ethylene flames. It is found that the time scale theory is well valid in the flame propagation and stabilization stages. The rates of energy generation and loss are then analyzed in the cavity. It is found that initially the local energy generation rate is relatively small, resulting in slow net energy accumulation in the cavity. Then the energy generation increases due to the intermittent flame propagation in the cavity, whereas the energy loss oscillates consistently since the burned gas leaves the cavity. Also, energy generation and loss are generally balanced in the cavity and all tend to zero after the flame is globally stabilized. The two methods present the characteristic time scales and energy balancing during the transient ignition process for the first time.

1. Introduction

The flow speed in a supersonic combustor typically is 1,000 m/s whereas the laminar flame speed of hydrocarbon fuels typically is 1 m/s or even lower [1]. Fuel mixing, ignition, and flame stabilization are difficult under such high-speed flow conditions. However, these physical-chemical processes are the key problems to design high-speed propulsion systems. Special methods are adopted to enhance ignition and improve flame stability, which are generally divided into two categories, i.e. increase flame burning velocity and decrease local flow speed. Specifically, flame speed can be increased by introducing laser-[2] or plasma-assisted igniters [3], seeding high reactivity radicals [4],

adding piloted flames [5], etc. However, practical use of the above methods is still relatively limited due to the difficulties in their implementation and active control. Conversely, Recirculation Zone (RZ) is widely used for aerodynamically stabilizing the flames in supersonic flows [6–8]. Both strut and cavity have been found to be effective devices to generate RZ for flame stabilization in combustors, as seen from the extensive experimental [9–11] and numerical [12–14] studies. Specifically, the quasi-steady state flame characteristics [15], combustion modes [16], and combustion instabilities [17] in cavity-based supersonic combustors have been extensively investigated with various cavity geometries and/or fueling schemes by Sun and Wang et al. All these studies provide valuable insights into cavity-type supersonic

* Corresponding author.

E-mail address: huangwei.zhang@nus.edu.sg (H. Zhang).

<https://doi.org/10.1016/j.apenergy.2020.114795>

Received 25 December 2019; Received in revised form 29 February 2020; Accepted 2 March 2020

Available online 10 March 2020

0306-2619/ © 2020 Elsevier Ltd. All rights reserved.

Nomenclature**Symbols**

$\bar{\rho}$	filtered density
\tilde{u}_j	filtered j -th velocity component
\bar{p}	filtered pressure
\tilde{T}	filtered temperature
$\tilde{\tau}_{ij}$	filtered viscous stress tensor
\tilde{H}	filtered total enthalpy
\tilde{h}_m	filtered sensible enthalpy of species m
\tilde{K}	filtered kinetic energy
\tilde{q}_j	filtered heat flux
\tilde{Y}_m	filtered mass fraction of species m
$\tilde{\omega}_m$	filtered reaction rate of species m
$\tilde{\omega}_T$	filtered heat release rate
δ_i	Kronecker delta function
\tilde{S}_{ij}	filtered strain rate tensor
$\Delta h_{f,m}^0$	standard enthalpy of formation of species m
N	total number of species
D	molecular diffusivity
Sc	Schmidt number
Sc_t	turbulent Schmidt number
Pr_t	turbulent Prandtl number
μ	dynamics viscosity
R_u	universal gas constant
M_m	molecular weight of species m
λ	heat conductivity
τ_{ij}^{sgs}	SGS stress tensor
μ_t	SGS dynamic viscosity
Δ	LES filter size
k_t	turbulent kinetic energy
h_j^{sgs}	SGS enthalpy flux
$Y_{j,m}^{sgs}$	SGS flux of species m
Da	Damköhler number
Da_{sgs}	SGS Damköhler number
τ_{sgs}	characteristic time scale of turbulence
τ_c	characteristic time scale of chemistry
Ma	Mach number
T^*	stagnation temperature
p^*	stagnation pressure
ϕ	global equivalence ratio
τ_{chem}	chemical time scale
τ_{mix}	mixing time scale
τ_{ind}	reaction induction time
τ_{RZ}	contact time

\bar{u}_{outer}	averaged velocity
\dot{m}_u, \dot{m}_b	mass flow rate
T_u^*, T_b^*	stagnation temperature
e_u^*, T_o^*	specific total energy
\dot{E}_{gen}	energy generation rate in the RZ
\dot{E}_{loss}	energy loss rate in the RZ
$\Delta \dot{E}$	net energy accumulation rate
s	stoichiometric mass ratio of oxidizer to fuel
Y_O^0	mass fraction of oxidizer in oxidizer stream
Y_F^0	mass fraction of fuel in fuel stream
Σ_{RZ}	closed surface of the RZ
\mathbf{n}	normal vector of Σ_{RZ}
u^+, v^+, w^+	velocity component flows in the RZ
u^-, v^-, w^-	velocity component flows out the RZ
$c_{p,1}, c_{p,2}$	heat capacity
z	mixture fraction
z_{st}	stoichiometric mixture fraction
ξ_{MR}	most reactive mixture fraction
$\nabla F, \nabla O$	gradient of fuel/oxidizer mass fraction
$sign, max$	sign/maximum function
m_{CV}	gas mass in the cavity
m_{CV-Ym}	mass of species m in the cavity
$\bar{\phi}_{CV}$	averaged equivalence ratio in the RZ
\bar{p}_{CV}	averaged pressure in the RZ
\bar{T}_{CV}	averaged temperature in the RZ
\bar{z}_{CV}	averaged mixture fraction in the RZ
\mathfrak{R}_{CV}	the cavity zone
V_{CV}	volume of the cavity
V_{RZ}	volume of the RZ
L_{RZ}	length of the RZ

Acronyms

RZ	recirculation zone
HBP	hot burned product
UCM	unburned combustible mixture
TSM	time scale method
EBM	energy balance method
LES	large eddy simulation
SGS	sub-grid scale
IDT	ignition delay time
TVD	total variation diminishing
PSR	perfectly stirred reactor
SFI	signed flame index
RANS	Reynolds-averaged Navier-Stokes

flames. Supersonic combustion research becomes increasingly popular in various countries like China [3,7,9,18], America [1,10,13], Russia [19,20], Japan [6,21], Australia [2,4], and Europe [12,22].

Moreover, initiation of turbulent diffusion combustion of gaseous fuels through autoignition and forced ignition has been reviewed in detail [23], wherein fundamentals of the associated turbulence-chemistry interaction are emphasized. Several canonical ignition problems, e.g. fuel jet in co-flow, mixing layer, opposed jet flow, and volumetric compression are analyzed at the low-speed flow regimes. However, the relevant discussion for supersonic flames is absent. Furthermore, although successful ignition and flame stabilization has been achieved experimentally using strut [11] or cavity [10] in supersonic flows, the underlying mechanisms are still not clear. Successful ignition and flame propagation in propulsion systems depend on many factors, e.g. the injection scheme, the ignition energy and position, the local flow speed, the combustor geometry [24,25]. Behind these factors there are two fundamental principles. The first is the competition between the

residence time of Hot Burned Product (HBP) and the reaction induction time of the fresh Unburned Combustible Mixture (UCM) in the RZ. The second is the balance between energy generation due to UCM reactions and energy loss from HBP to UCM in the RZ. An improved understanding on ignition and flame stabilization mechanisms may actually give insights into enhanced design of robust supersonic combustors.

A model supersonic combustor equipped with a strut for fuel injection and wall cavities for flame stabilization is investigated by a highly resolved Large Eddy Simulation (LES) in this study. Low-order methods for the foregoing time scale and energy balance in high-speed flames are developed and applied to the simulated flame. Hereafter, these two methods are termed as TSM (time scale method) and EBM (energy balance method), respectively. The LES results provide the input data for the analysis using the low-order models of flame autoignition and stabilization. The TSM provides us an estimation of where autoignition first occurs in the mixture fraction space and what the order of magnitude of the autoignition time scale is. The EBM explains

the development of flame autoignition observed in the LES. Hence, the present work contributes to the understanding on flame autoignition and stabilization mechanisms in supersonic flows based on two different methods.

The novelties of our current work include the following scientific and application aspects. Firstly, flame autoignition in shock-laden flows is studied here. The role of the shock compression in initiating the flame is explored, which has not been clearly understood as mentioned above [23]. Secondly, the proposed low-order models act as the useful engineering tools to provide us the detailed evolutions of the time scale and energy balance relevant to transient flame autoignition and propagation. They can be further applied for analyzing other flame dynamics problems (e.g. extinction or instability). Thirdly, from application point of view, the combustor considered here is characterized by joint arrangement of strut and cavity, which has not been extensively studied. Most of the studied supersonic combustor configurations contain strut only or cavity only [19]. This configuration is expected to significantly increase the efficiency of energy utilization from hydrocarbon fuel combustion, through promoting the flame ignition and enhancing the flame stabilization. Lastly, the EBM is derived from the universal energy conservation law, which makes it extendable for other types of heat engines that may be fueled with various chemical fuels and/or operate under various conditions. Understanding the energy conversion and conservation characteristics of such devices, in turn, helps us improve the combustor design.

The rest of the paper is structured as below. Numerical methods, including LES governing equations and Sub-Grid Scale (SGS) models, numerical schemes and chemical kinetics are presented in Section 2. Details about the model combustor, including the computational configuration and simulation conditions for LES are described in Section 3. The TSM and EBM for flame stabilization in recirculation zones are developed in Section 4. Evolutions of the time scale and energy balance in the flame ignition are presented in Section 5. Conclusions are drawn in Section 6.

2. Governing equations and numerical methods

2.1. LES governing equations

The LES governing equations of mass, momentum, energy, and species mass fractions are solved for fully compressible, multi-component reacting flows [26]. They read

$$\frac{\partial \bar{\rho}}{\partial t} + \frac{\partial}{\partial x_j} (\bar{\rho} \tilde{u}_j) = 0, \quad (1)$$

$$\frac{\partial}{\partial t} (\bar{\rho} \tilde{u}_i) + \frac{\partial}{\partial x_j} (\bar{\rho} \tilde{u}_i \tilde{u}_j + \bar{p} \delta_{ij} - \tilde{\tau}_{ij} + \tau_{ij}^{\text{sgs}}) = 0, \quad (2)$$

$$\frac{\partial}{\partial t} (\bar{\rho} \tilde{H}) - \frac{\partial \bar{p}}{\partial t} + \frac{\partial}{\partial x_j} (\bar{\rho} \tilde{H} \tilde{u}_j + \tilde{q}_j - \tilde{u}_j \tilde{\tau}_{ij} + h_j^{\text{sgs}}) = \bar{\omega}_T, \quad (3)$$

$$\frac{\partial}{\partial t} (\bar{\rho} \tilde{Y}_m) + \frac{\partial}{\partial x_j} \left(\bar{\rho} \tilde{Y}_m \tilde{u}_j - \bar{p} D \frac{\partial \tilde{Y}_m}{\partial x_j} + Y_{j,m}^{\text{sgs}} \right) = \bar{\omega}_m, \quad (4)$$

where t is time, x is spatial coordinate, $\bar{\rho}$ is filtered density, \tilde{u}_j is filtered j -th velocity component, \bar{p} is filtered pressure, δ_{ij} is Kronecker delta function, $\tilde{\tau}_{ij}$ is viscous stress tensor, $\tilde{H} = \tilde{h} + \tilde{K}$ is filtered total enthalpy (filtered sensible enthalpy \tilde{h} plus filtered kinetic energy $\tilde{K} = \frac{1}{2} \sum_{i=1}^3 \tilde{u}_i^2$), \tilde{q}_j is filtered heat flux, \tilde{Y}_m is filtered mass fraction of m -th species, and $\bar{\omega}_m$ is the filtered reaction rate of m -th species. The filtered heat release rate $\bar{\omega}_T = -\sum_{m=1}^N \bar{\omega}_m \Delta h_{f,m}^0$, where $\Delta h_{f,m}^0$ is the standard enthalpy of formation for m -th species, and N is the total number of species. Mass diffusivity is modelled as $D = \mu / \bar{\rho} Sc$, where $Sc = 0.7$ is Schmidt number, μ is dynamic viscosity of the mixture. The filtered pressure \bar{p} is determined by (neglecting its correlation with density fluctuations)

$$\bar{p} = \bar{\rho} R_u \tilde{T} \sum_{m=1}^N \frac{\tilde{Y}_m}{M_m}, \quad (5)$$

where $R_u = 8.314 \text{ J}/(\text{mol}\cdot\text{K})$ is the universal gas constant, \tilde{T} is filtered temperature, and M_m is the molecular weight of m -th species.

The filtered viscous stress tensor in Eq. (2), $\tilde{\tau}_{ij}$, is expressed as

$$\tilde{\tau}_{ij} = \mu \left(\tilde{S}_{ij} - \frac{1}{3} \tilde{S}_{kk} \delta_{ij} \right), \quad (6)$$

where $\tilde{S}_{ij} = \frac{\partial \tilde{u}_i}{\partial x_j} + \frac{\partial \tilde{u}_j}{\partial x_i}$ is the filtered strain rate tensor. The filtered heat flux \tilde{q}_j in Eq. (3) is

$$\tilde{q}_j = -\lambda \frac{\partial \tilde{T}}{\partial x_j}, \quad (7)$$

where λ is thermal conductivity.

The SGS stress tensor τ_{ij}^{sgs} is [27]

$$\tau_{ij}^{\text{sgs}} = -\mu_t \left(\tilde{S}_{ij} - \frac{1}{3} \tilde{S}_{kk} \delta_{ij} \right) + \frac{2}{3} \bar{\rho} k_t \delta_{ij} \quad (8)$$

where $\mu_t = C_k \bar{\rho} \Delta \sqrt{k_t}$ is the SGS dynamic viscosity, $C_k = 0.094$ is a model constant [28], Δ is the filter size estimated as the cube root square of the LES cell volume. The turbulent kinetic energy k_t in Eq. (8) is determined by solving the following transport equation [28]

$$\frac{\partial}{\partial t} (\bar{\rho} k_t) + \frac{\partial}{\partial x_j} (\bar{\rho} \tilde{u}_j k_t) - \frac{\partial}{\partial x_j} \left[(\mu + \mu_t) \frac{\partial k_t}{\partial x_j} \right] = -\tau_{ij}^{\text{sgs}} \frac{\partial \tilde{u}_i}{\partial x_j} - \frac{C_e \bar{\rho} k_t^{3/2}}{\Delta}, \quad (9)$$

where $C_e = 1.048$ [28] is a model constant. Compared with the zero-equation algebraic models (e.g. Smagorinsky model), the one-equation eddy viscosity SGS model is expected to give more accurate results because it relaxes local equilibrium assumption between the SGS energy production and dissipation, originally introduced in the zero-equation model. This assumption may not be valid in high-Reynolds-number flows and/or with insufficient grid resolution [28]. Hence, this model provides an independent SGS velocity scale with little increase in computational cost [29].

The SGS enthalpy flux h_j^{sgs} in Eq. (3) is related to the gradient of the filtered enthalpy

$$h_j^{\text{sgs}} = -\frac{\mu_t}{Pr_t} \frac{\partial \tilde{h}}{\partial x_j} \quad (10)$$

where $Pr_t = 0.9$ is the turbulent Prandtl number [30]. Moreover, the SGS scalar flux of m -th species in Eq. (4) is modelled as

$$Y_{j,m}^{\text{sgs}} = -\frac{\mu_t}{Sc_t} \frac{\partial \tilde{Y}_m}{\partial x_j}, \quad (11)$$

where $Sc_t = 0.4$ is the turbulent Schmidt number [30].

The turbulence-chemistry interaction is not considered in this study, and the filtered reaction rates of individual species $\bar{\omega}_m$ in Eq. (4) are calculated based on the filtered species mass fractions, density, and temperature (termed as laminar chemistry approach hereafter). Similar treatment for supersonic combustion also has been used, e.g. in Refs. [22,31,32]. Accurate predictions of temperature, velocity, and nitrogen mole fraction with experimental data have been achieved in the ramp-stabilized supersonic hydrogen-air diffusion flame [31]. Good agreements of the predicted mean temperatures and mean species concentrations with the experimental data also have been achieved in supersonic lifted jet flames as well as in the supersonic combustion of near-wall boundary layers [32]. Specifically, the autoignition positions in both two cases are reasonably well captured in Ref. [32]. Therefore, the laminar chemistry approach is expected to be sufficient to capture the ignition dynamics in our case using LES with high grid resolution, which is further justified in Section 3.1.

A skeletal mechanism consists of 20 species and 36 reactions are adopted for ethylene combustion [33]. A detailed validation of this

mechanism in terms of laminar flame speed, adiabatic temperature, and Ignition Delay Time (IDT) has been performed by Liu et al. [34] with experimental data [35,36] or the detailed USC mechanism [37]. Good predictions are seen in terms of laminar flame speed and adiabatic temperature at different equivalence ratios (0.5–1.8) under 298 K and 1 atm. The IDT is also well captured at different pressures (1 atm and 3 atm) and initial temperatures (833–1430 K). This mechanism has been used to investigate the transient autoignition process in a cavity-based combustor [34].

2.2. Numerical methods

The LES governing equations are solved in a density-based multi-component reactive flow solver *RYrhoCentralFoam*, which is developed based on a fully compressible flow solver, *rhoCentralFoam*, in OpenFOAM 5.0 package [38]. The finite volume method is used for spatial discretization of Eqs. (1)–(4). The solution of momentum and energy equations uses an operator-splitting approach [38]. Specifically, in the first step, an explicit predictor equation is solved for the convection of conserved variables. In the second step, an implicit corrector equation for the diffusion of primitive variables is solved. Moreover, second-order semi-discrete, non-staggered, Godunov-type central-upwind scheme developed by Kurganov, Noelle and Petrova [39] (termed as KNP scheme hereafter) is used for the convection terms in momentum and energy equations. This enables the formation of flux interpolations considering its transport in any directions due to the compressible flow and wave propagation and avoid the explicit need for a Riemann solver. It is shown that the KNP scheme is competitive in accuracy with the other numerical schemes, e.g. Roe scheme [38].

Detailed chemistry calculations can be performed with *RYrhoCentralFoam* through Eq. (4), and the convection terms are predicted using a TVD (total variation diminishing) scheme to ensure the scalar boundness. The diffusive terms in Eqs. (1)–(4) are split into orthogonal and non-orthogonal parts to minimize the non-orthogonality error. Second-order Gauss scheme with linear interpolation is used for the orthogonal part and surface interpolation of variable normal gradients is applied for the non-orthogonal part. Implicit second-order Crank-Nicolson scheme is applied for the time discretization. The maximum Courant number is set to be 0.1, which approximately corresponds to the physical time step of 10^{-9} s. The solver has been applied and validated with both supersonic combustion [40,41] and detonative combustion [42]. The similar strategy has also been used by other groups, e.g. by Wu [8] and Li [43] for supersonic hydrogen flames in the DLR strut combustor. The velocity, pressure and overall flame behaviors are predicted reasonably well in their respective studies [8,43].

3. Problem specification

3.1. Physical model

A model supersonic combustor equipped with both strut and cavity is investigated in this study, which is schematically shown in Fig. 1. Ethylene (C_2H_4) is parallelly injected into the airflow from a strut injector with 8 convergent-divergent nozzles. The diameter of each nozzle is 1.5×10^{-3} m at the throat and 2.2×10^{-3} m at the exit. The strut has a length of 0.07 m and a width of 0.012 m, which is placed 0.069 m downstream of the combustor entrance. Two wall cavities are oppositely mounted at 0.179 m downstream of the combustor entrance. Each cavity is 0.024 m in length and 0.006 m in depth with an inclination angle of 45° at the rear wall. The combustor is a rectangular duct with a cross-section area of $0.04 \text{ m} \times 0.055 \text{ m}$ and a total length of 0.424 m.

Currently the experimental data from this specific combustor are not available for comparisons with the LES. Therefore, the following efforts are made to ensure the soundness of our results to the largest extent. Firstly, the numerical solver has been well validated and applied in different problems of high-speed combustion, including strut supersonic combustor [40,41], supersonic auto-igniting hydrogen flames [44] and rotating detonative combustion [42]. Good accuracies are observed in various quantities from the above work. Secondly, very fine mesh is used to resolve most of the kinetic energy. A *posterior* analysis is made to examine the sufficiency of the current mesh. Thirdly, with the foregoing fine mesh resolution, the model-free method, i.e. laminar chemistry approach, is used for predicting turbulent combustion. This is helpful to alleviate the uncertainties or errors in the combustion modelling due to the non-universal or *ad hoc* sub-models. Therefore, the results from the highly-resolved LES are expected to be accurate and reliable.

47.4 million hexahedral cells are used to discretize the computational domain in Fig. 1. For better capturing the fine turbulence structures and flame front, the grid is locally refined at all the solid walls, the strut jet-wake zone, and the central combustion zone. Fig. 2 shows the local enlarged grids around the fuel injector and the cavity. The thin pink lines are the grid lines, while the thick black lines are solid walls. The minimum grid size is 9.375×10^{-5} m around the injector and in the jet-wake zones, and 1.0×10^{-4} m in the cavity.

A *posterior* examination of the grid resolution is performed based on LES results. The spatially-mean y^+ values are 0.1 near the cavity, 0.9 near the strut, and 0.5 near the combustor walls. Therefore, the near-wall turbulence is well-resolved. Furthermore, a well-known criterion to measure the LES quality is the ratio of the SGS viscosity to the molecular viscosity, i.e. [45,46]

$$\mu_E = \frac{\mu_t}{\mu} \quad (12)$$

Fig. 3(a) shows the scatter plots of μ_E versus the filtered heat release

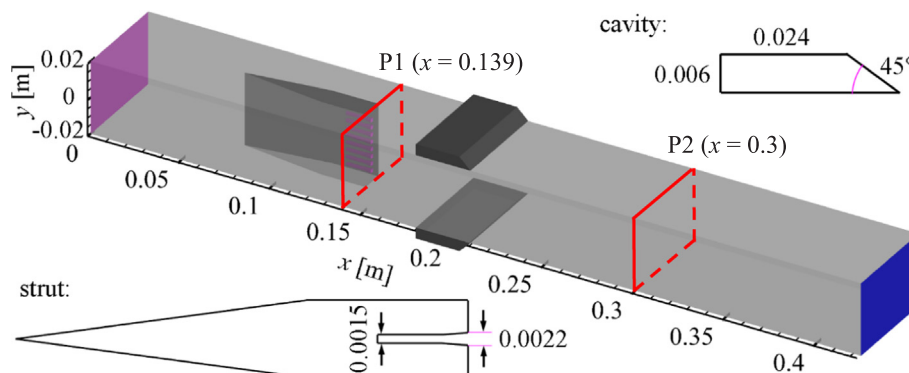


Fig. 1. Schematic of the model supersonic combustor. The domain bounded between the two cross-sections P1 ($x = 0.139$ m, where is the injector exit) and P2 ($x = 0.3$ m, behind the cavity) is used for visualizations in Figs. 6, 8, and 9.

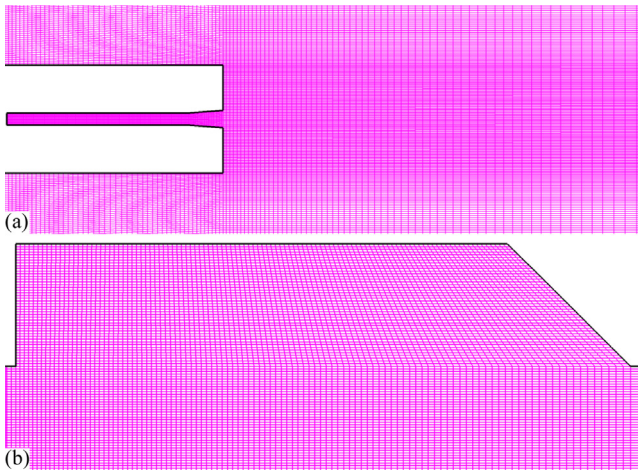


Fig. 2. Local enlarged grids around (a) the fuel injector and (b) the cavity.

rate ($\bar{\omega}_T$, in $[\text{W}/\text{m}^3]$) at the combustor center plane when the flame has stabilized. For most of the regions with significant heat release rate (e.g. $\bar{\omega}_T \geq 1 \times 10^9 \text{ W}/\text{m}^3$), the corresponding values of μ_E are less than 2 (bounded by the black dashed box B1 in Fig. 3a). Only a small region with $\bar{\omega}_T$ typically lower than $1 \times 10^9 \text{ W}/\text{m}^3$ is observable for $4 \leq \mu_E \leq 7$ (bounded by the pink dashed box B2 in Fig. 3a). Therefore, based on the criterion in Ref. [46], in our LES the relevant combustion regions are highly resolved.

The flame resolution is evaluated through the validity of the laminar chemistry approach, i.e. directly using filtered reactive scalar values (e.g. reactant concentration, temperature) to calculate the filtered species reaction rates. The SGS Damköhler number, Da_{sgs} , is calculated as [46]

$$Da_{sgs} = \frac{\tau_{sgs}}{\tau_c} = \left(\frac{\bar{\rho} C_s^2 \Delta^2}{\mu_t} \right) \left(\frac{\bar{\rho}}{|\bar{\omega}_{H_2O}|} \right) = \frac{C_s^2 \Delta^2}{\mu_t} |\bar{\omega}_{H_2O}|, \quad (13)$$

where τ_{sgs} is the characteristic time of the smallest resolved structure [47] and τ_c is the characteristic time of chemistry [48]. $C_s = 0.15$ is a constant, $\bar{\omega}_{H_2O}$ is the reaction rate of H_2O . The condition of $Da_{sgs} \ll 1$ is required to minimize the errors induced by the reactive fluctuations in estimating the resolved chemical reaction rates [49]. It means that the characteristic chemical time scales are sufficiently resolved and the effects of the SGS fluctuations on the filtered reaction rates are negligible [50]. Fig. 3(b) shows the three-dimensional contours of the instantaneous Da_{sgs} after the fuel injector. It is seen that the highest Da_{sgs} is 0.0125 in the entire combustor, which is much less than unity. Hence, our LES with this resolution is also adequate to capture the ignition dynamics without considering the SGS fluctuations of reactive scalars.

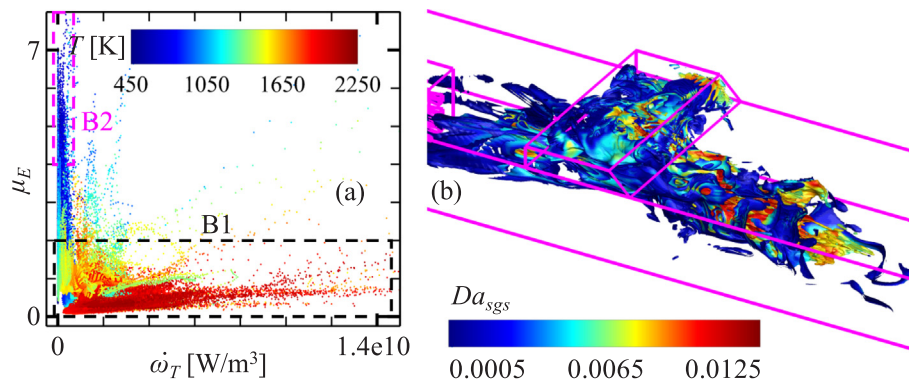


Fig. 3. Evaluation on the grid resolution: (a) scatter plots of μ_E versus $\bar{\omega}_T$ colored by temperature and (b) contours of instantaneous SGS Damköhler number Da_{sgs} .

3.2. Simulation conditions

Mach number (Ma) at the combustor entrance is 2.5, whereas the air stagnation temperature (T^*) and pressure (p^*) are 1,700 K and 1.5 MPa, respectively. These conditions approximately correspond to a flight Mach number of 6.5. The air mass flow rate is 1.0 kg/s. Ethylene is used to mimic the major dissociation products of kerosene after flowing over the cooling channel slotted along the combustor walls [34]. Mach number of ethylene at the injector exit is 2.0. The stagnation temperature and pressure of ethylene are 600 K and 1.07 MPa, respectively. The global equivalence ratio ϕ is 0.4. The vitiated air is provided by a pre-combusted heater, which consists of 23.3% O_2 , 7.6% H_2O , 12.5% CO_2 , and 56.6% N_2 by mass. The specific inlet conditions of both oxidizer and fuel are detailed in Table 1.

Initially, the flow field in the domain is assumed to be quiescent, whereas the temperature is initialized with the static temperature of air stream (941 K). Air and ethylene enter the combustor simultaneously at the initiation of the simulation.

4. Low-order theories for flame autoignition and stabilization

4.1. Characteristic time scale analysis

Fig. 4 shows a schematic of TSM in the RZ created by, e.g. a bluff body. The RZ is regarded as a high-temperature zone filled with HBP, which mixes with UCM at the interface through diffusion and convection. The UCM is heated to reach the autoignition temperature, and a stable flame can occur after an induction distance [51]. Hence, whether a stable flame is achievable after the bluff body depends on whether the UCM is sufficiently heated by the HBP immediately after the strut. Furthermore, the total heat transferred depends on the time that HBP interacts with UCM.

The total time for UCM to be ignited, hereafter denoted as τ_{chem} , is dominated by two components, i.e. the time within which the UCM mixes with the HBP (denoted as τ_{mix}), and the induction time for UCM ignition (denoted as τ_{ind}). Therefore,

$$\tau_{chem} = \tau_{mix} + \tau_{ind} \quad (14)$$

Moreover, the time that the HBP in the RZ interacts with the UCM in a distance of the length of the RZ (denoted as L_{RZ}), τ_{RZ} , is calculated as

$$\tau_{RZ} = L_{RZ} / \bar{u}_{outer}, \quad (15)$$

where \bar{u}_{outer} is the average velocity of the UCM in the main stream. If $\tau_{RZ} > \tau_{chem}$, UCM can be ignited, resulting in a globally stable flame downstream. Conversely, if τ_{ind} increases under some unfavorable conditions (e.g. off-flammability limit, sudden decrease in temperature and/or pressure of the air stream), the flame front would be blown off from the RZ. If τ_{ind} or τ_{chem} is large enough, global flame extinction occurs. Furthermore, according to the experimental observations [52], generally $\tau_{mix} \ll \tau_{ind}$. This assumption is also widely adopted in other

Table 1
Inlet conditions of air and ethylene.

inlet	T^* [K]	p^* [MPa]	Ma	Y_{O_2}	Y_{H_2O}	Y_{CO_2}	Y_{N_2}	$Y_{C_2H_4}$	ϕ
Vitiated air	1,700	1.5	2.5	0.233	0.076	0.125	0.566	0.0	0.4
Fuel (ethylene)	600	1.07	2.0	0.0	0.0	0.0	0.0	1.0	

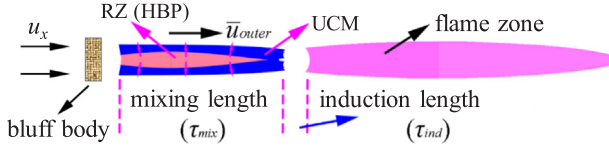


Fig. 4. Schematic of the time scale analysis. The red zone denotes the recirculation zone filled with hot burned product (HBP), the blue zone denotes the surrounding unburned combustible mixture (UCM), and the pink zone denotes the flame zone.

studies of supersonic flame stabilization, e.g. in Refs. [6,7,9,10,11,13], and is of good validity in our case due to the following reasons. Firstly, the speed is low while the temperature is high for HBP in the RZ. The typical Mach number of HBP in the RZ is lower than 0.3 (hence HBP is of low-compressibility and even incompressible) while the typical temperature is 1,200 K or higher after shock-induced ignition occurs. This can be verified from Figs. 6, 8, and 9 shown later. However, the speed is much higher while the temperature is much lower for UCM in the main flow. The large velocity gradient results in strong species convection between HBP and UCM, whereas the large temperature gradient leads to strong diffusion effect. The both effects enhance mixing between HBP and UCM. Secondly, τ_{mix} is generally tens of microseconds in our *posterior* calculations based on the LES results. However, τ_{ind} generally ranges from 200 to 1,800 μs under proper mixture fractions (e.g. 0.015–0.045, the typical mixture fractions in the cavity), and can get much higher under fuel-leaner or richer conditions as shown in Fig. 11. Therefore, τ_{mix} can be neglected in Eq. (14), and the critical condition for flame stabilization is approximated as

$$\tau_{RZ} \approx \tau_{ind}. \quad (16)$$

In high-Reynolds-number flows like supersonic flows, L_{RZ} is comparable to the characteristic length of the flame-holder. As such, according to Eqs. (15) and (16), flame stability may be improved, e.g. by increasing the characteristic dimensions of the flame-holders (e.g. the strut height, the cavity length), decreasing the air inflow velocity while increasing its pressure, or accelerating the chemical reactions (e.g. introducing hot burned exhaust gas, plasma).

Therefore, TSM is a time scale based theory, which is consistent with the Damköhler (Da) number based criterion [53] for extinction. The Da number is defined as the ratio of the fluid timescale to the chemical timescale, and $Da = 1$ is the critical condition to determine the initiation of flame extinction. However, the Da number is a global quantity, which cannot provide the detailed time scale evolutions for the transient ignition and flame stabilization process. Specifically, an ignition Da number has been defined to quantify the effect of turbulence on the early ignition characteristics [54], and a limiting global Da number has been found for each fuel (under which the ignition probability is about zero) [55]. However, these Da numbers are only applicable for the initial mixtures. Conversely, the two time scales we

define above vary with the local thermo-physical conditions, are applicable to the entire process, i.e. from occurrence of flame kernel, flame propagation and flame stabilization.

4.2. Energy balance analysis

Fig. 5 shows a schematic of EBM, in which the RZ is treated as a Perfectly Stirred Reactor (PSR) with homogeneous temperature and compositions [56]. Combustion in the RZ is presumably divided into two sequential processes, i.e. (a) mixing process of UCM and HBP at an infinitely small time scale; (b) chemical reactions at finite rate. Within this finite reaction time, some of the partially burned gas is recirculated back, denoted as process (c) in Fig. 5. Take the entire RZ as a control volume, heat generation comes from the combustion of the local mixture, whereas energy loss is due to the total energy difference between HBP leaves and UCM enters the RZ. Flame stabilization is dominated by the balance between the energy generation and loss. Note that the heat transfer between the gas and flame-holder walls, heat conduction between HBP and UCM, and radiative heat loss are not considered. In EBM, in the statistical sense, we have that

- For the ignition process, heat generation rate (\dot{E}_{gen}) is generally larger than the loss rate (\dot{E}_{loss}). Energy is accumulated in the RZ, which finally results in successful ignition and flame propagation;
- For the flame stabilization process, \dot{E}_{gen} is approximately equal to \dot{E}_{loss} . Heat is dynamically balanced in the RZ with flame fluctuations;
- For the flame extinction process, \dot{E}_{gen} is generally smaller than \dot{E}_{loss} . Heat in the RZ itself decreases continuously. Local flame extinction first occurs in the RZ, which further transits to global extinction.

It is assumed that the UCM flows into the RZ at a mass flow rate of \dot{m}_u and stagnation temperature of T_u^* . The instantaneous mass flow rate of HBP originally in the RZ is \dot{m}_b at stagnation temperature of T_b^* . After process (a) shown in Fig. 5, the mixture at mass flow rate of $(\dot{m}_u + \dot{m}_b)$ and stagnation temperature of T_m^* is obtained. In process (b), the mixture separates into two streams. One is partly reacted and recirculated back in process (c). Its mass flow rate is \dot{m}_{RZ} and stagnation temperature is T_b^* . The reminder stream is more sufficiently reacted and leaves the RZ at a mass flow rate of $(\dot{m}_u + \dot{m}_b - \dot{m}_{RZ})$ and stagnation temperature of T_o^* .

The total heat release rate in the RZ, \dot{E}_{gen} , can be obtained from

$$\dot{E}_{gen} = \iiint_{V_{RZ}} \bar{\omega}_T dx dy dz, \quad (17)$$

where V_{RZ} is the volume of the RZ.

If the flame is stabilized or the RZ reaches a statistically steady state, the mass flow rates at which the flows enter and leave the RZ are balanced, i.e.

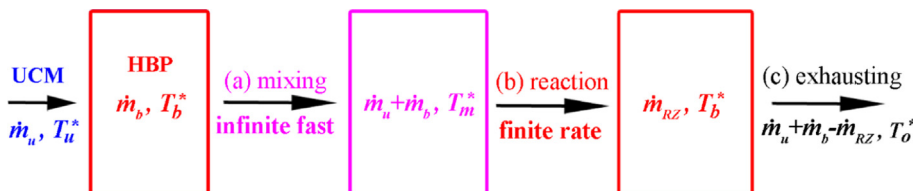


Fig. 5. Schematic of the energy balance analysis. Process (a) is the infinitely fast mixing between HBP and UCM, (b) is the finite rate reaction of UCM, and (c) is the exhausting of HBP.

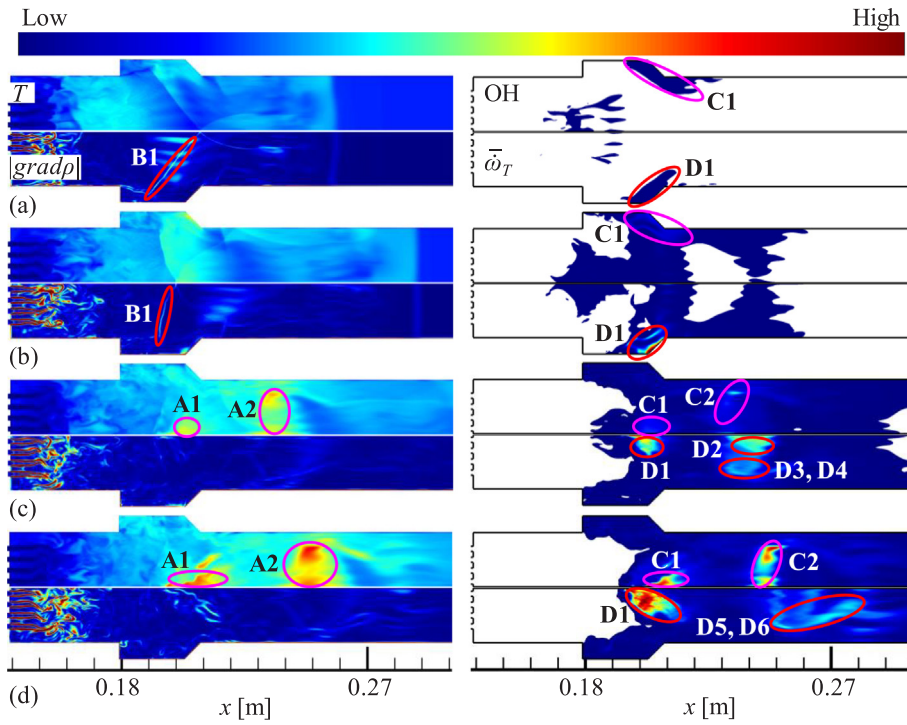


Fig. 6. Time evolution of the scalar fields at: (a) 0 μ s, (b) 30 μ s, (c) 60 μ s, and (d) 90 μ s. For each instant, from left to right and from upper to lower, temperature (range: 450–2650 K), OH mass fraction (range: 1×10^{-6} –0.016), magnitude of density gradient (range: 0–200 kg/m⁴), and heat release rate (range: 1×10^7 – 8×10^{10} W/m³) are shown.

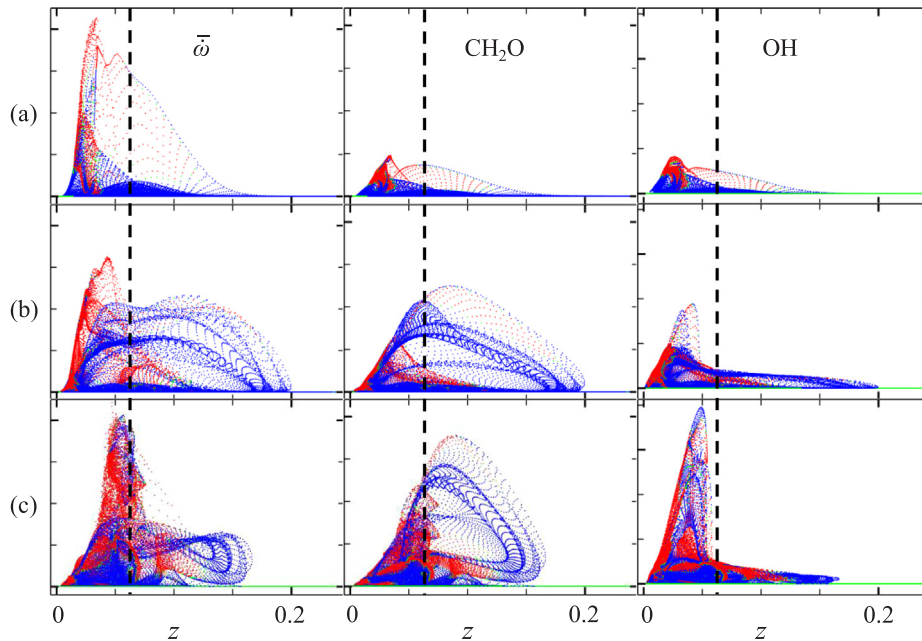


Fig. 7. Scatter plots of heat release rate (first column, range: 0 – 8×10^{10} W/m³), CH₂O (second column, range: 0 – 0.02) and OH (third column, range: 0 – 0.012) mass fractions in mixture fraction space at: (a) 30 μ s, (b) 60 μ s, and (c) 90 μ s. The dashed lines denote $z_{st} = 0.0636$, whereas the red dots: premixed combustion, blue dots: diffusion combustion, green dots: non-reactive.

$$\dot{m}_u = \dot{m}_{RZ} \quad (18)$$

The closed surface of the RZ is denoted as Σ_{RZ} with unit normal vector of \mathbf{n} . The net mass flow rate across the surface is zero, i.e.

$$\iint_{\Sigma_{RZ}} \rho(\mathbf{U} \cdot \mathbf{n}) d\Sigma = \iiint_{V_{RZ}} \text{div}(\rho \mathbf{U}) dV = 0 \quad (19)$$

where $\mathbf{U} = (u, v, w)$ is the velocity vector. According to the Gauss theorem, Eq. (19) can be re-cast into

$$\iiint_{V_{RZ}} \rho \left(\frac{\partial u}{\partial x} + \frac{\partial v}{\partial y} + \frac{\partial w}{\partial z} \right) dx dy dz = 0. \quad (20)$$

The velocity components can be decomposed into two parts. For the gas flows into the RZ, they are denoted as u^+ , v^+ , and w^+ , respectively. Conversely, for the gas flows out of the RZ, they are denoted as u^- , v^- , and w^- , respectively. Equation (20) is then rearranged as

$$\iiint_{V_{RZ}} \rho \left[\left(\frac{\partial u^+}{\partial x} + \frac{\partial v^+}{\partial y} + \frac{\partial w^+}{\partial z} \right) - \left(\frac{\partial u^-}{\partial x} + \frac{\partial v^-}{\partial y} + \frac{\partial w^-}{\partial z} \right) \right] dx dy dz = 0 \quad (21)$$

Therefore, the mass flow rate through Σ_{RZ} is

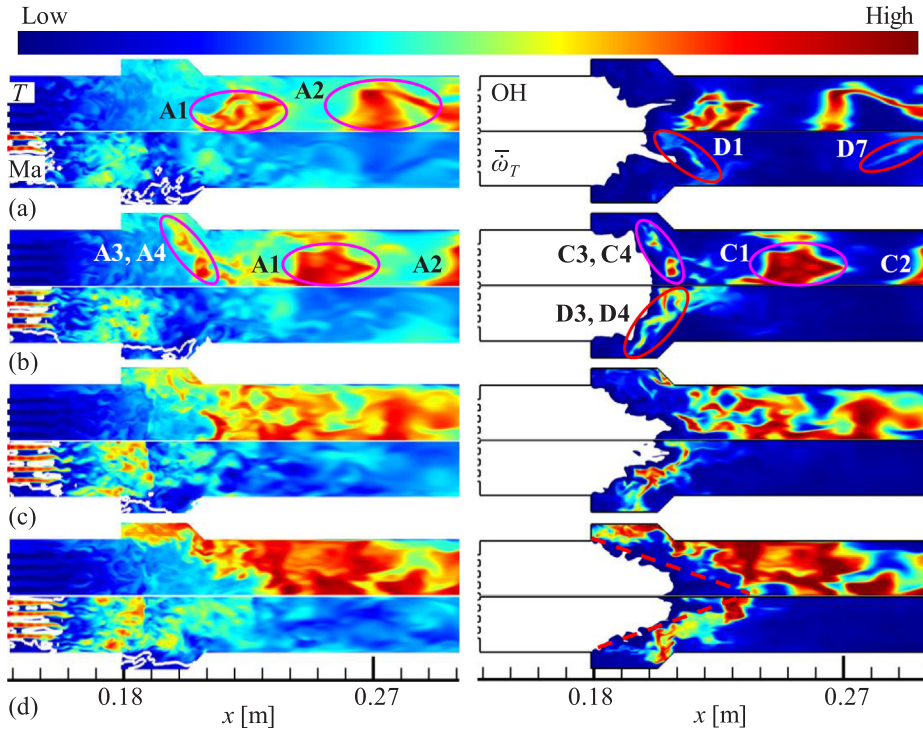


Fig. 8. Time evolution of the scalar fields at: (a) 130 μ s, (b) 170 μ s, (c) 220 μ s, and (d) 270 μ s. For each instant, from left to right and from upper to lower, temperature (range: 450–2650 K), OH mass fraction (range: 1×10^{-6} –0.016), Mach number (range: 0–2.4) superimposed with iso-lines of $u_x = 0$, and heat release rate (range: 1×10^7 – 8×10^{10} W/m³) are shown.

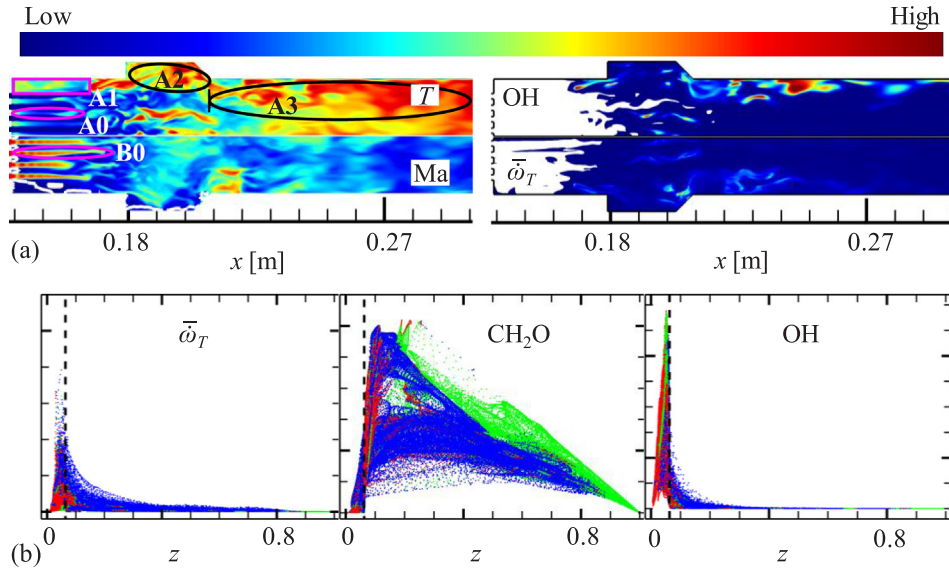


Fig. 9. Instantaneous (a) scalar fields and (b) scatter plots in the mixture fraction space at 1070 μ s. The fields and their corresponding ranges in Fig. 9(a) are same to those in Fig. 8, and those in Fig. 9(b) are same to those in Fig. 7.

$$\begin{aligned} \dot{m}_u &= \iiint_{V_{RZ}} \rho \left(\frac{\partial u^+}{\partial x} + \frac{\partial v^+}{\partial y} + \frac{\partial w^+}{\partial z} \right) dx dy dz \\ &= \frac{1}{2} \iiint_{V_{RZ}} \rho \left(\left| \frac{\partial u}{\partial x} \right| + \left| \frac{\partial v}{\partial y} \right| + \left| \frac{\partial w}{\partial z} \right| \right) dx dy dz \end{aligned} \quad (22)$$

The energy loss due to the total energy difference between UCM and HBP, \dot{E}_{loss} , is then calculated as

$$\dot{E}_{loss} = \dot{m}_u (c_{p,2} T_o^* - c_{p,1} T_u^*), \quad (23)$$

where $c_{p,1}$ and $c_{p,2}$ are respectively the specific heat capacities of UCM and HBP. Therefore, the energy balance equation in the RZ is

$$\begin{aligned} &\iiint_{V_{RZ}} \bar{\omega}_T dx dy dz \\ &= \frac{c_{p,2} T_o^* - c_{p,1} T_u^*}{2} \iiint_{V_{RZ}} \rho \left(\left| \frac{\partial u}{\partial x} \right| + \left| \frac{\partial v}{\partial y} \right| + \left| \frac{\partial w}{\partial z} \right| \right) dx dy dz. \end{aligned} \quad (24)$$

5. Results and discussion

5.1. Highly-resolved LES of flame ignition and stabilization

5.1.1. Formation of the shock-induced autoignition spots

Fig. 6 shows the evolutions of temperature, magnitude of density gradient, hydroxyl (OH) mass fraction, and heat release rate at $t = 0$ –90 μ s. Note that $t = 0$ μ s corresponds to the instant at which the

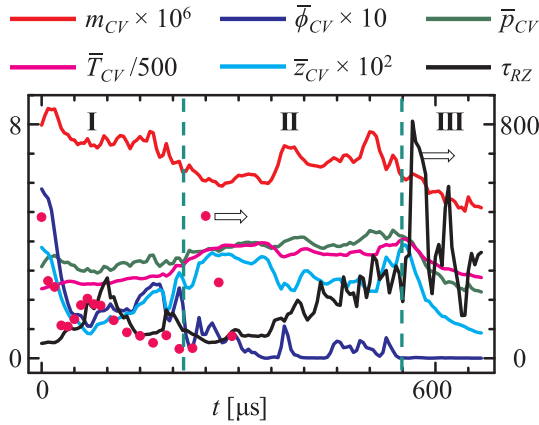


Fig. 10. Time evolution of gas thermophysical properties and residence time in the cavity. The scatter points are the corresponding ignition delay time. Units are: m_{CV} in kg, \bar{p}_{CV} in MPa, \bar{T}_{CV} in K, τ_{RZ} and τ_{ind} in μ s. Only τ_{RZ} and τ_{ind} use the right legend. The green dashed lines are two characteristic times ($t = 220$ and 550μ s).

auto-igniting hot spot occurs, based on the increased intermediate species mass fraction in the combustor, e.g. OH. OH is formed in reaction layers and consumed by slow recombination reactions [57], which is a marker of hot products in high speed flows. It can widely exist in non-reactive regions due to species transport but not limited to thin reaction layers in the combustor [58].

At $t = 0 \mu$ s, the supersonic air from the entrance reaches and impinges on the cavity rear walls. Two bow shocks are formed due to strong compression near the rear of the cavities, which is indicated by zone B1 in Fig. 6(a). These two shocks intersect at the combustor centerline at $x \approx 0.208$ m. Gas temperature in the cavity is increased (reaches about 1,200 K) after the shocks. However, it is still not sufficient to induce ignition immediately. OH is low and $\bar{\omega}_T$ is small, which are only observable near the cavity rear walls, indicated by zones C1 and D1 in Fig. 6(a), respectively.

At $t = 30 \mu$ s, gas in the cavity is further blocked and the bow shocks almost evolve into normal shocks in front of the cavity rear walls (zone B1 in Fig. 6b). The two shocks intersect at $x \approx 0.198$ m in the combustor centerline. The highest temperature near the cavity rear wall reaches about 1,750 K, which is slightly higher than air stagnation temperature. Hence, noticeable combustion heat release has occurred before this instant, which is confirmed by the distributions of OH and $\bar{\omega}_T$ indicated by zones C1 and D1 in Fig. 6(b), respectively. Three auto-igniting hot spots are formed at the two cavity rear walls and the shock intersection point. However, the highest $\bar{\omega}_T$ indicates that reaction in the auto-igniting hot spots is not strong.

At $t = 60 \mu$ s, the hot spots at the combustor center (indicated by zone A1 in Fig. 6c) is transported downstream (zone A2 in Fig. 6c). The

bow shocks are weakened by combustion and many shocklets featured by considerable density gradient are formed in the cavity. The concentration of OH radical along the hot spots is increased. There are four isolated islands with noticeable $\bar{\omega}_T$, i.e. zone D1 at the combustor center, zone D2 some distance behind, zones D3 and D4 transported from the hot spots at the rear wall of the upper and lower cavities. The latter three, zones D2, D3 and D4, tend to merge with each other.

At $t = 90 \mu$ s, larger area with high temperature (e.g. above 2,200 K) is seen in the combustor in two separated zones A1 and A2 in Fig. 6(d). The high temperature zones are developed and transported downwards to ignite more fuel/air mixtures around zones A1 and A2. Zones D2, D3, and D4 in the previous instant merge into zones D5 and D6 (one in upper half and the other in lower half of the combustor) with significant $\bar{\omega}_T$. Zone D1 grows with time, whereas zones D5 and D6 are dissipated due to thermal loss and/or radical transport to their surroundings.

It is revealing to examine the autoignition process in mixture fraction space. The mixture fraction (z) is defined as in Ref. [26] and the stoichiometric value is $z_{st} = 0.0636$. Fig. 7 shows the scatter plots of $\bar{\omega}_T$, CH_2O , and OH mass fractions versus z at three instants. Formaldehyde (CH_2O) is formed in the preheat layer of hydrocarbon flames from the initial fuel decomposition reactions and is consumed in reaction layer [59]. It is an important precursor radical prior to autoignition [60]. The points in Fig. 7 are colored by the Signed Flame Index (SFI), which is defined as [61]

$$SFI = \text{sign}(\nabla F \cdot \nabla O) \cdot \max[\text{sign}(\bar{\omega}_T - [\bar{\omega}_T] \cdot \beta), 0], \quad (25)$$

where the sign function $\text{sign}(x)$ returns +1 if $x \geq 0$, and returns -1 if $x < 0$, whilst the maximum function $\max(x,y)$ returns the larger one between x and y . ∇F and ∇O are the gradients of the fuel and oxidizer mass fractions, respectively. $[\bar{\omega}_T]$ is the volume average of $\bar{\omega}_T$ in the entire computational domain, and β is a small fraction, say 1% in this study. Based on our numerical experiments, slightly smaller or larger values of β would not cause any appreciable change in the results due to the sharp gradient of heat release in the combustion zone. Therefore, $[\bar{\omega}_T] \cdot \beta$ can be viewed as a threshold to identify the non-zero $\bar{\omega}_T$. It is obvious from Eq. (25) that

$$SFI = +1, \quad \text{if } \nabla F \cdot \nabla O \geq 0 \quad \text{and} \quad \bar{\omega}_T \geq [\bar{\omega}_T] \cdot \beta$$

$$SFI = -1, \quad \text{if } \nabla F \cdot \nabla O < 0 \quad \text{and} \quad \bar{\omega}_T \geq [\bar{\omega}_T] \cdot \beta$$

$$SFI = 0, \quad \text{if } \bar{\omega}_T < [\bar{\omega}_T] \cdot \beta$$

Therefore, SFI is an indicator for various situations: premixed flame ($SFI = +1$), diffusion flame ($SFI = -1$), and non-reactive flows ($SFI = 0$).

At $t = 0 \mu$ s (not shown), $\bar{\omega}_T$, CH_2O , and OH mass fractions are zero. At the next instant, say 1μ s later, however, they start to increase. At $t = 30 \mu$ s, there is an obvious increase in the heat release $\bar{\omega}_T$. The mixture fraction corresponding to the highest $\bar{\omega}_T$ is lower than z_{st} , i.e. lies in the fuel-lean side. This value of z is termed as the most reactive

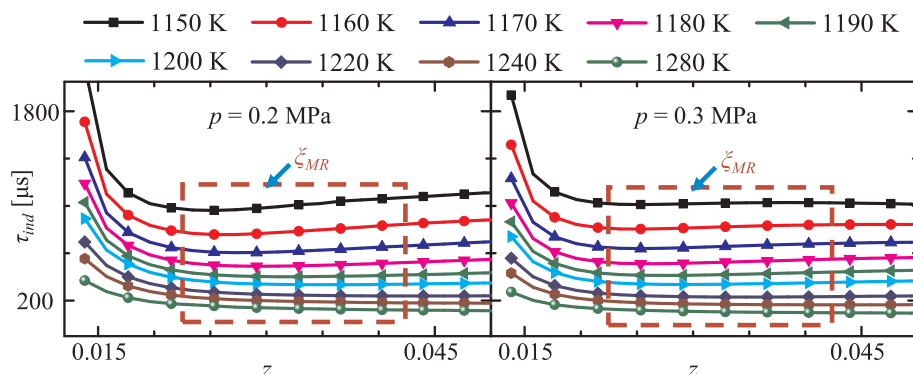


Fig. 11. Calculations of ignition delay time in homogeneous ethylene/air mixtures. The dashed box bounds the range of the most reactive mixture fraction.

mixture fraction (ξ_{MR}) [23], and is analyzed in Section 5.2. Premixed combustion is dominant at this instant. At $t = 60 \mu\text{s}$, $\bar{\omega}_T$ has two extremum values because there are four discontinuous combustion zones spatially, one in the upstream zone D1 and the other three in the downstream zones D2, D3 and D4 (see Fig. 6c). At $t = 90 \mu\text{s}$, the higher CH_2O but lower OH in zones D5 and D6 (denoted by the blue dots) indicates that strong decomposition reactions of C_2H_4 are dominant.

The autoignition process in this period (0–90 μs) is characterized by the formation of bow shocks due to supersonic flow compression at the cavity rear walls, and the formation of discrete igniting hot spots due to these shocks. Significant reactions can only undergo in a narrow range of mixture fraction (from 0 to 0.2) and the premixed and diffusion combustion modes are comparable. The cavity firstly induces the formation of bow shocks (and thus auto-igniting hot spots) at the rear walls, then provides a high temperature (due to deceleration of the supersonic air inflow) recirculation zone favorable to the growth of the initial flame. The strut in front of the cavity provides a preliminary low-speed flow for the cavity (see Fig. 8). Hence, the combination of strut and cavity improves the ignition ability in supersonic flows compared with pure strut or cavity, which has been experimentally observed in, e.g. Refs. [9,11].

Also note that both strength and location of the shocks adjust with the development of the flow field. The shocks at the cavity rear walls may even disappear after the flame is globally stabilized (see Fig. 9). The behavior of the shocks and the shock-induced igniting spots shows strong dynamics in the ignition, which is more complex than simple geometries, e.g. the supersonic jet flame with hot co-flow [46]. A transient bow shock is found to be created by the flame, which allows for the first autoignition of the hydrogen/air mixture. The interaction between the shock and flame shows strong intermittency and periodicity but does not entirely vanish. The measurements of autoignition lengths in a low-speed jet flame [62] show that turbulent mixing delays autoignition. However, in our case turbulent mixing enhances ignition in the cavity through increasing the fuel temperature and the mixture homogeneity while decreasing the UCM ignition delay due to the mixing with intermediate species. Similar positive feedback between the cavity mixing and heat release also has been observed in the work of Wang et al. [63], in which the interactions between bow shocks and fuel mixing/combustion are numerically investigated.

5.1.2. Flame stabilization

Fig. 8 shows the evolutions of temperature, Mach number, OH mass fraction, and heat release rate at $t = 130\text{--}270 \mu\text{s}$. At $t = 130 \mu\text{s}$, the local flame in zone D1 reaches at the side wall of the combustor, grows both longitudinally and transversely. Zones D5 and D6 with local flames in the previous instant merge into a single zone D7, which grows about two thirds of the full height of the combustor in Fig. 8(a). Gas speed in the cavity is low and the RZ shows strong spatial discontinuity. However, both $\bar{\omega}_T$ and OH are low in the cavity at this instant.

At $t = 170 \mu\text{s}$, the high-temperature zones A3 and A4 occur again in front of the cavity rear walls in Fig. 8(b). The thermo-chemical conditions, e.g. gas temperature and intermediate species, are more in favor of local re-ignition of fuel/air mixtures in the cavity compared with previous instants (e.g. $t = 0\text{--}90 \mu\text{s}$) due to the previous burning of gas in the cavity. It is seen that the downstream zone C1 with high OH mass fraction exists after zones D3 and D4, which are featured with strong $\bar{\omega}_T$. Zone A2 is transported further downstream.

At $t = 220 \mu\text{s}$, the local high-temperature zones almost join together and form an extensive area with high temperature after the cavity in Fig. 8(c). The cavity is partly filled with high temperature gas as well, but are not accomplished with significant $\bar{\omega}_T$. Within 170–220 μs , it is found that HBP in the rear part of cavity has a tendency to be transported upstream due to the flow recirculation. At $t = 270 \mu\text{s}$, the cavity is full of HBP and intermediate species, e.g. OH in Fig. 8(d). The high temperature zones after the cavity become spatially more continuous. Gas in the front part of the cavity is ignited by the recirculated HBP

from the rear part.

The scatter plots of $\bar{\omega}_T$, CH_2O and OH in mixture fraction space (not shown for brevity) indicate that premixed combustion becomes more dominant as the flame evolves. The highest $\bar{\omega}_T$ increases stably while the highest OH tends to stable in this period. Furthermore, as most of the region after the cavity section is ignited while the cavity is only partly ignited, CH_2O is low, which indicates that flame propagation but not re-ignition is dominated in this period.

The autoignition process in this period (130–270 μs) is characterized by propagation of the local flame (induced by hot spots in previous instants) both downstream and upstream. Premixed combustion is found to be dominant. After a long time ($\sim 800 \mu\text{s}$) of HBP backward convection towards the strut, the combustion field finally reaches a statistically steady state. Fig. 9(a) shows the contours of T , Ma , OH and $\bar{\omega}_T$ at $t = 1070 \mu\text{s}$. Fig. 9(b) shows the scatter plots of $\bar{\omega}_T$, CH_2O and OH against z at this instant. It is found that the region between two adjacent injectors (e.g. zone A0 in Fig. 9a) and the region between the injector and combustor wall (zone A1) are preheated to above 1,300 K accompanied with weak decomposition of C_2H_4 , and therefore with low $\bar{\omega}_T$. HBP is stabilized in the entire cavity as indicated by zone A2. Behind the cavity, HBP is seen in a wide band close to the combustor wall indicated by zone A3. The Mach trains are clearly seen in each separated supersonic ethylene jet with a long tail (circled by zone B0). The supersonic jets then break up and partly entrained into the cavity, which is continuously ignited by HBP. The remainder of the jets is transported downstream to sustain combustion in the center region. At this instant, flame is stabilized in the cavity and fully established in the combustor. The scatters in Fig. 9(b) acquires the expected shape for diffusion combustion [23].

5.2. Low-order analysis of flame ignition and stabilization

It is found in Figs. 8 and 9 that the speed of the recirculating gas in the cavity is low, compared to that of the incoming air stream. Hence, the entire cavity presumably acts as the recirculation zone for ignition and flame stabilization. The TSM and EBM are respectively applied to study the evolutions of gas thermodynamics in the cavity during the ignition process in Sections 5.2.1 and 5.2.2.

5.2.1. Time scale analysis

Fig. 10 shows the evolutions of the volume-averaged gas thermo-physical properties (e.g. m_{CV} , $\bar{\phi}_{CV}$, \bar{p}_{CV} , \bar{T}_{CV} , and \bar{z}_{CV}) and residence time (τ_{RZ}) in the cavity zone (denoted as \mathfrak{R}_{CV}). The total mass (m_{CV}) and the mass of interested species (m_{CV-Y_m}) are calculated respectively as

$$m_{CV} = \iiint_{\mathfrak{R}_{CV}} \rho dx dy dz, \quad (26)$$

$$m_{CV-Y_m} = \iiint_{\mathfrak{R}_{CV}} \rho Y_m dx dy dz. \quad (27)$$

A nominal global equivalence ratio in the cavity ($\bar{\phi}_{CV}$) is calculated based on $m_{CV-C_2H_4}$ and m_{CV-O_2} . The volume-averaged temperature and pressure in the cavity are respectively calculated as

$$\bar{T}_{CV} = \iiint_{\mathfrak{R}_{CV}} T dx dy dz / V_{CV}, \quad (28)$$

$$\bar{p}_{CV} = \iiint_{\mathfrak{R}_{CV}} p dx dy dz / V_{CV}, \quad (29)$$

where $V_{CV} = 8.91 \times 10^{-6} \text{m}^3$ is the volume of the cavity. The volume-averaged mixture fraction, \bar{z}_{CV} , is calculated as

$$\bar{z}_{CV} = \frac{s \frac{m_{CV-C_2H_4}}{m_{CV}} - \frac{m_{CV-O_2}}{m_{CV}} + Y_O^0}{s Y_F^0 + Y_O^0} \quad (30)$$

where $s = 24/7$ is the stoichiometric mass ratio of O_2 to C_2H_4 , $Y_O^0 = 0.233$ is O_2 mass fraction in the oxidizer stream, and $Y_F^0 = 1.0$ is C_2H_4 mass fraction in the fuel stream. The IDT of UCM in the cavity is calculated under the conditions of \bar{z}_{CV} , \bar{T}_{CV} and \bar{p}_{CV} using homogeneous

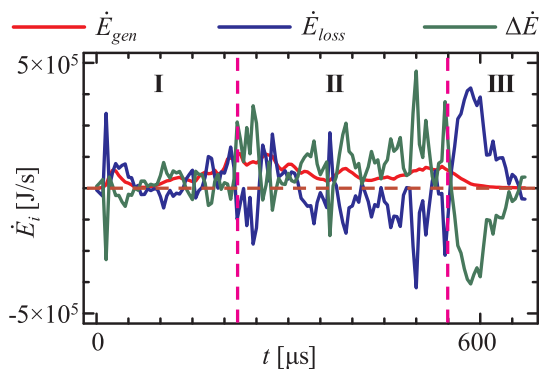


Fig. 12. Time evolution of energy balance in the cavity. The pink dashed lines are two characteristic times ($t = 220$ and $550 \mu\text{s}$).

PSR model, in which the autoignition is assumed to occur when $T \geq 1,800$ K. Selecting different temperature threshold values would not cause significant change in the predicted IDT as temperature increases rapidly at ignition [64].

In Fig. 10, it is found that remarkable fuel ($\bar{\phi}_{CV} = 0.579$, larger than the global equivalence ratio 0.4) is entrained into the cavity and hence leads to premixed UCM at $t = 0 \mu\text{s}$. From $t = 0$ – $220 \mu\text{s}$, as autoignition occurs in the cavity, \bar{T}_{CV} increases gradually, which leads to pronounced thermal expansion in the cavity. This may prevent the fuel further entrainment into the cavity, and hence $\bar{\phi}_{CV}$ decreases. \bar{z}_{CV} is lower than z_{st} (0.0636) but is close to the most reactive mixture fraction ξ_{MR} , which is shown in Fig. 11. τ_{RZ} increases rapidly due to the flow blockage induced by the bow shocks at the cavity rear walls before $t = 70 \mu\text{s}$. However, τ_{RZ} is generally smaller than τ_{ind} before this instant. This is not contradictory to the time scale theory in Section 4.1 (requires $\tau_{RZ} \geq \tau_{ind}$) as there are no flames in the cavity currently. After $t = 70 \mu\text{s}$, $\tau_{RZ} \geq \tau_{ind}$ is well satisfied.

From $t = 220$ – $550 \mu\text{s}$, m_{CV} decreases oscillatorily. On one hand, increased \bar{T}_{CV} generally leads to enhanced gas thermal expansion (see the increased \bar{p}_{CV}). This prevents the surrounding gas to enter the cavity whereas the cavity gas is easier to be transport out of the RZ. On the other hand, the gas before the cavity is not fully ignited (before $t = 550 \mu\text{s}$), part of which enters the cavity at relatively high density. The low $\bar{\phi}_{CV}$ at $t = 250$ – $270 \mu\text{s}$ leads to $\tau_{ind} > \tau_{RZ}$. The TSM only accounts for the ignition of fuel/oxidizer at their initial forms (i.e. $\text{C}_2\text{H}_4/\text{O}_2$). However, in real flames, there are many intermediate species, e.g. OH, H, O, CH_2O , HCO. These reactive radicals may accelerate the chemistry of $\text{C}_2\text{H}_4/\text{O}_2$ and hence decrease the IDT. Also, the radical reactions may be dominant when the concentration of C_2H_4 and/or O_2 is low. However, this fact is not considered when calculate τ_{ind} of UCM in TSM. After $t = 270 \mu\text{s}$, τ_{ind} is missing due to excessive low $\bar{\phi}_{CV}$. Successful ignition is not achievable in the homogeneous PSR calculations.

It is seen that before $t = 550 \mu\text{s}$, gas properties in the cavity (e.g. m_{CV} , \bar{T}_{CV} , $\bar{\phi}_{CV}$, \bar{z}_{CV}) show strong fluctuations with flame propagation against the main flow in front of the cavity. After then, these quantities tend to reach statistically steady state (not shown after $t = 670 \mu\text{s}$ in Fig. 10). It is noteworthy that although $\bar{\phi}_{CV}$ varies remarkably in the ignition process, \bar{z}_{CV} does not. From Eq. (30), it is seen that \bar{z}_{CV} depends on not only $m_{CV-\text{O}_2}$ and $m_{CV-\text{C}_2\text{H}_4}$, but also m_{CV} . Furthermore, \bar{z}_{CV} is smaller than z_{st} in the ignition process.

In Figs. 7 and 9, it is found that CH_2O , OH, and $\bar{\omega}_T$ reach their maximums preferentially at the mixture fractions that are separated from the stoichiometric line. The most reactive mixture fraction is the one at which the reaction rate is the maximum [23]. A series of homogeneous PSR calculations are performed, with initial conditions of temperature and pressure close to those at the early ignition time in Fig. 10. Specifically, the temperature is 1,150–1,280 K, the pressure is 0.2 MPa and 0.3 MPa (typical values of \bar{p}_{CV} in Fig. 10), and air

composition is same as that at the combustor entrance. For $T \geq 1,280$ K the IDT is short (tens of microseconds) and ignition is readily achieved. Furthermore, \bar{T}_{CV} is hardly lower than 1,150 K, because the minimum \bar{T}_{CV} in the entire ignition process is 1,190 K (only occurs at $t = 0 \mu\text{s}$).

Fig. 11 shows the calculated τ_{ind} versus z at 0.2 and 0.3 MPa and 1,150–1,280 K. ξ_{MR} is indicated by the dashed box. The determination of ξ_{MR} is not rigorous as the minimum τ_{ind} is relatively broad [23]. It is seen that the curves are relatively flat in the shown range of mixture fraction after $z \approx 0.0225$, especially at higher temperatures and higher pressures. Here, we take ξ_{MR} in a range of 0.0225–0.04. It is seen that \bar{z}_{CV} at most instants in Fig. 10 locates in this range. At some instants, \bar{z}_{CV} is slightly lower than 0.0225, which may be due to the following reasons. First, as seen in Fig. 11, the higher the initial temperature is, the lower limit of ξ_{MR} that first occurs. At most instants, \bar{T}_{CV} is remarkably higher than the highest T in Fig. 11 (1,280 K). The lower limit of ξ_{MR} may be smaller than 0.0225 when T is higher. Second, \bar{z}_{CV} is volume-averaged in the entire cavity. However, the cavity may be not homogeneously mixed as an idealized PSR. The actual z at the ignition front may be higher than \bar{z}_{CV} . Anyhow, ξ_{MR} provides an estimation of where autoignition firstly occurs in the mixture fraction space and what the order of magnitude of the actual autoignition time scale is.

5.2.2. Energy balance analysis

The specific total energy of the gas flows in (e_i^*) or out of (e_o^*) the cavity is calculated as

$$e_i^* = c_{p,i} T_i^* = \iiint_{G_i} \rho c_p T^* dx dy dz / \iiint_{G_i} \rho dx dy dz, \quad (31)$$

where G_i is the gas flows into or out of the cavity, and e_i^* is the corresponding specific total energy.

Fig. 12 shows the evolutions of energy generation and loss rates as well as the net energy ($\Delta \dot{E} = \dot{E}_{gen} - \dot{E}_{loss}$) accumulation rate in the cavity. At $t = 0 \mu\text{s}$, \dot{E}_{gen} is slightly above 0, indicating an initiation of combustion heat release. Total energy of the gas entering the cavity is larger than that leaving it, leading to negative \dot{E}_{loss} . This means that through interaction with the surrounding, the total energy in the cavity is increased. This is because that the supersonic air inflow ($T^* = 1,700\text{K}$) reaches at the cavity rear wall at this instant, while the original gas in the cavity is relatively cold ($T^* < 941\text{K}$). Short after $t = 0 \mu\text{s}$, both \dot{E}_{gen} and \dot{E}_{loss} increase rapidly. At $t = 30 \mu\text{s}$, significant heat release is achieved through the spontaneous reactions in the cavity itself. Once chemical reactions are initiated, gas temperature in the cavity increases rapidly. However, as it is shown in Fig. 6, flame cannot be stabilized immediately after its first occurrence in the cavity. Weak combustion and even local flame extinction may occur due to instantaneous large \dot{E}_{loss} (e.g. $t = 30$ – $40 \mu\text{s}$). The EBM, to some degree, explains the flame intermittency in the cavity at the early phase of ignition.

Before $t = 550 \mu\text{s}$, \dot{E}_{loss} is negative at most time. Energy in the cavity is featured with continuous and strong oscillatory accumulation process. After $t = 320 \mu\text{s}$, reactions in the cavity reach the steady-state and hence \dot{E}_{gen} varies mildly with time. This leads to the moderate variation of thermophysical properties of the gas flows out of the cavity. However, this is not the case for the gas flows in due to the flame propagation upstream against the main flow in the combustor in front of the cavity (see Fig. 8). After $t = 550 \mu\text{s}$, \dot{E}_{gen} drops towards zero because $\bar{\omega}_T$ in the cavity is low when the combustor finally reaches the statistically steady-state (see Fig. 9a). \dot{E}_{loss} becomes positive means that the cavity is able to generate energy to the main flow after a long time of energy accumulation. However, at about $t = 1,000 \mu\text{s}$ (not shown), \dot{E}_{loss} also tends to be 0 as \dot{E}_{gen} .

Note that although TSM and EBM are developed to investigate the unsteady ignition process in the recirculation zones resulted from bluff body type flame-holders, they are of practical significance in a more general sense. They may be also used to study the unsteady flame extinction process and the statistically steady state flame stabilization. For

the highly unsteady processes, e.g. flame ignition and extinction, highly resolved LES is desired to provide the transient input data (see Eqs. (16) and (24)) for both the TSM and EBM. The evolution of intermediate species also may be obtained using the transient analysis method with skeletal or detailed chemical kinetics. However, for quasi-steady problems like stabilized flames, steady RANS may be able to provide the accurate input data for the two low-order models, which provide detailed quantitative insights into the mechanisms of flame ignition, stabilization and extinction. Understanding these flame characteristics helps us improve the combustor design. For example, if the flame extinguishes in our case, we will know the reason based on the transient energy balance analysis. We can improve our flame stabilizer (strut and cavity combination) design to enhance energy generation and weaken energy loss in the recirculation zone.

Moreover, the EBM we developed is applicable to other types of energy conversion and utilization devices fueled with other type of fuels, but not limited to our specific combustor fueled with ethylene. Firstly, the strut/cavity combination is effective for flame stabilization (and hence for the conversion of chemical energy of fuels to the thermal energy and kinetic energy of the working fluid) in supersonic flows. In spite of the differences in combustor configurations and/or operating conditions, the energy conversion and conservation processes in other internal combustion engines, e.g. laser-induced plasma ignition engine [3], spark-assisted ignition engines [65,66], are similar for chemical fuels. Secondly, although ethylene is used as fuel in our case, the application of the EBM is general for other gaseous fuels (e.g. hydrogen, methane, natural gas). For liquid fuels (e.g. hydrocarbon-type kerosene, ethanol) that are widely used as practical energy resources, the EBM can also be extended, through considering the heat loss term due to the liquid evaporation into the energy equation.

6. Conclusions

The time scale and energy balance methods are developed in this work, which are then applied to investigate the flame autoignition and propagation of supersonic ethylene flames simulated with highly resolved large eddy simulation. The two methods can provide us the insights into the characteristic time scales and energy balancing during the transient ignition process.

From the numerical results, one can find that flame kernels are initiated from the auto-igniting hot spots induced by supersonic flow compression at the cavity rear wall and the intersection of bow shocks in the combustor center. The local flames developed from the hot spots then propagate both downstream and upstream, and premixed combustion mode is dominant. It is also seen that the flame is finally stabilized downstream of the strut injectors and now diffusion combustion is dominant.

The evolutions of the two time scales are calculated in the ignition process of the ethylene flames. It is found that from 0 to 220 μs , when the autoignition hot spots arise in the cavity, the average temperature increases whereas the average equivalence ratio and mixture fraction decrease. From 220 to 550 μs , at different stages of flame propagation in the cavity, gas properties in the cavity show strong fluctuations. It is found that the time scale theory is well valid in the flame propagation dominated process within the lean flammability of ethylene / oxygen mixture. After about 550 μs , gas properties in the cavity tend to be stable. The most reactive mixture fraction ranges from 0.0225 to 0.04, which is lower than the stoichiometric value 0.0636, but is close to the average value in the cavity.

The rates of energy generation and loss are then analyzed for the ignition process in the cavity. It is found that from 0 to 220 μs , the local energy generation rate is small, resulting in slow net energy accumulation in the cavity. From 220 to 550 μs , the energy generation increases due to the intermittent flame propagation in the cavity, whereas the energy loss oscillates consistently since the hot product leaves the cavity. This results in strong fluctuation in net energy accumulation.

After 550 μs , the energy generation rate is negligibly small, whereas the energy loss rate is positive but also tends to be zero after about 1,000 μs . Energy generation and loss are generally balanced in the cavity after the flame is globally stabilized.

Lastly, starting from the underlying universal energy conversation law, the energy balance method is applicable to analyze the unsteady flame ignition and extinction processes and the statistically steady state flame stabilization. It is also extendable towards a broader range, including other types of heat engines fueled with various chemical fuels and operate under various conditions. Understanding the energy conversion and conservation characteristics of such devices, in turn, helps us improve the combustor design.

CRedit authorship contribution statement

Zhiwei Huang: Conceptualization, Methodology, Software, Formal analysis. **Huangwei Zhang:** Writing - review & editing, Supervision, Project administration.

Declaration of Competing Interest

The authors declare that they have no known competing financial interests or personal relationships that could have appeared to influence the work reported in this paper.

Acknowledgements

The computational work for this article was fully performed on resources of the National Supercomputing Center, Singapore (<https://www.nscg.org/>).

References

- [1] Urzay J. Supersonic combustion in air-breathing propulsion systems for hypersonic flight. *Annu Rev Fluid Mech* 2018;50:593–627.
- [2] Brieschenk S, O'Byrne S, Kleine H. Laser-induced plasma ignition studies in a model scramjet engine. *Combust Flame* 2013;160:145–8.
- [3] Cai Z, Zhu J, Sun M, Wang Z, Bai XS. Ignition processes and modes excited by laser-induced plasma in a cavity-based supersonic combustor. *Appl Energy* 2018;228:1777–82.
- [4] McGuire JR, Boyce RR, Mudford NR. Radical-farm ignition processes in two-dimensional supersonic combustion. *J Propuls Power* 2008;24:1248–57.
- [5] Wei B, Xu X, Yan M, Shi X, Yang Y. Study on integrated aeroramp injector/gas-pilot flame in a supersonic combustor. *J Propuls Power* 2012;28:486–95.
- [6] Nakaya S, Hikichi Y, Nakazawa Y, Sakaki K, Choi M, Tsue M, et al. Ignition and supersonic combustion behavior of liquid ethanol in a scramjet model combustor with cavity flame holder. *Proc Combust Inst* 2015;35:2091–9.
- [7] Yuan Y, Zhang T, Yao W, Fan X, Zhang P. Characterization of flame stabilization modes in an ethylene-fueled supersonic combustor using time-resolved CH* chemiluminescence. *Proc Combust Inst* 2017;36:2919–25.
- [8] Wu K, Zhang P, Yao W, Fan X. Computational realization of multiple flame stabilization modes in DLR strut-injection hydrogen supersonic combustor. *Proc Combust Inst* 2019;37:3685–92.
- [9] Sun MB, Zhong Z, Liang JH, Wang HB. Experimental investigation on combustion performance of cavity-strut injection of supercritical kerosene in supersonic model combustor. *Acta Astronaut* 2016;127:112–9.
- [10] Ma L, Lei Q, Wu Y, Xu W, Ombrello TM, Carter CD. From ignition to stable combustion in a cavity flameholder studied via 3D tomographic chemiluminescence at 20 kHz. *Combust Flame* 2016;165:1–10.
- [11] Sathiyamoorthy K, Danish TH, Srinivas J, Manjunath P. Experimental investigation of supersonic combustion in a strut-cavity based combustor. *Acta Astronaut* 2018;148:285–93.
- [12] Fureby C, Nordin-Bates K, Petterson K, Bresson A, Sabelnikov V. A computational study of supersonic combustion in strut injector and hypermixer flow fields. *Proc Combust Inst* 2015;35:2127–35.
- [13] Potturi AS, Edwards JR. Large-eddy/Reynolds-averaged Navier-Stokes simulation of cavity-stabilized ethylene combustion. *Combust Flame* 2015;162:1176–92.
- [14] Huang Z, He G, Wang S, Qin F, Wei X, Shi L. Simulations of combustion oscillation and flame dynamics in a strut-based supersonic combustor. *Int J Hydrogen Energy* 2017;42:8278–87.
- [15] Sun MB, Wang ZG, Liang JH, Geng H. Flame characteristics in supersonic combustor with hydrogen injection upstream of cavity flameholder. *J Propuls Power* 2008;24:688–96.
- [16] Wang H, Wang Z, Sun M, Wu H. Combustion modes of hydrogen jet combustion in a cavity-based supersonic combustor. *Int J Hydrogen Energy* 2013;38:12078–89.

- [17] Wang ZG, Sun MB, Wang HB, Yu JF, Liang JH, Zhuang FC. Mixing-related low frequency oscillation of combustion in an ethylene-fueled supersonic combustor. *Proc Combust Inst* 2015;35:2137–44.
- [18] Huang W, Yan L. Numerical investigation on the ram-scam transition mechanism in a strut-based dual-mode scramjet combustor. *Int J Hydrogen Energy* 2016;41:4799–807.
- [19] Seleznev RK, Surzhikov ST, Shang JS. A review of the scramjet experimental data base. *Prog Aerosp Sci* 2019;106:43–70.
- [20] Goyné CP, Rodríguez CG, Krauss RH, McDaniel JC, McClinton CR. Experimental and numerical study of a dual-mode scramjet combustor. *J Propuls Power* 2006;22:481–9.
- [21] Takita K, Abe N, Masuya G, Ju Y. Ignition enhancement by addition of NO and NO₂ from a N₂/O₂ plasma torch in a supersonic flow. *Proc Combust Inst* 2007;31(II):2489–96.
- [22] Gerlinger P, Nold K, Aigner M. Influence of reaction mechanisms, grid spacing, and inflow conditions on the numerical simulation of lifted supersonic flames. *Int J Numer Methods Fluids* 2010;102:1357–80.
- [23] Mastorakos E. Ignition of turbulent non-premixed flames. *Prog Energy Combust Sci* 2009;35:57–97.
- [24] An B, Wang Z, Yang L, Li X, Zhu J. Experimental investigation on the impacts of ignition energy and position on ignition processes in supersonic flows by laser induced plasma. *Acta Astronaut* 2017;137:444–9.
- [25] Bao X, Sahu A, Jiang Y, Badawy T, Xu H. Flame kernel evolution and shock wave propagation with laser ignition in ethanol-air mixtures. *Appl Energy* 2019;233–234:86–98.
- [26] Poinot T, Veynante D. *Theoretical and numerical combustion*. 2nd Edition. Flourtown, United States: R.T. Edwards; 2005.
- [27] Smagorinsky J. General circulation experiments with the primitive equations. *Mon Weather Rev* 1963;91:99–164.
- [28] Yoshizawa A, Horiuti K. A statistically-derived subgrid-scale kinetic energy model for the large-eddy simulation of turbulent flows. *J Phys Soc Japan* 1985;54:2834–9.
- [29] Fureby C, Tabor G, Weller HG, Gosman AD. A comparative study of subgrid scale models in homogeneous isotropic turbulence. *Phys Fluids* 1997;9:1416–29.
- [30] Pitsch H, Steiner H. Large-eddy simulation of a turbulent piloted methane/air diffusion flame (Sandia flame D). *Phys Fluids* 2000;12:2541–54.
- [31] Fulton JA, Edwards JR, Cutler A, McDaniel J, Goyné C. Turbulence/chemistry interactions in a ramp-stabilized supersonic hydrogen–air diffusion flame. *Combust Flame* 2016;174:152–65.
- [32] Gao Z, Jiang C, Lee CH. On the laminar finite rate model and flamelet model for supersonic turbulent combustion flows. *Int J Hydrogen Energy* 2016;41:13238–53.
- [33] Li S, Varatharajan B, Williams F. The chemistry of ethylene ignition for application to pulse-detonation engines. In: 36th AIAA/ASME/SAE/ASEE Jt. Propuls. Conf. Exhib., American Institute of Aeronautics and Astronautics; 2000.
- [34] Liu X, Cai Z, Tong Y, Zheng H. Investigation of transient ignition process in a cavity based scramjet combustor using combined ethylene injectors. *Acta Astronaut* 2017;137:1–7.
- [35] Jomaas G, Zheng XL, Zhu DL, Law CK. Experimental determination of counterflow ignition temperatures and laminar flame speeds of C₂–C₃ hydrocarbons at atmospheric and elevated pressures. *Proc Combust Inst* 2005;30:193–200.
- [36] Kumar K, Mittal G, Sung CJ, Law CK. An experimental investigation of ethylene/O₂/diluent mixtures: Laminar flame speeds with preheat and ignition delays at high pressures. *Combust Flame* 2008;153:343–54.
- [37] http://ignis.usc.edu/Mechanisms/USC-Mech%20II/USC_Mech%20II.htm n.d.
- [38] Greenshields CJ, Weller HG, Gasparini L, Reese JM. Implementation of semi-discrete, non-staggered central schemes in a collocated, polyhedral, finite volume framework, for high-speed viscous flows. *Int J Numer Methods Fluids* 2010;63:1–21.
- [39] Kurganov A, Noelle S, Petrova G. Semidiscrete central-upwind schemes for hyperbolic conservation laws and Hamilton-Jacobi equations. *SIAM J Sci Comput* 2001;23:707–40.
- [40] Huang Z, Zhang H. Numerical investigations of mixed supersonic and subsonic combustion modes in a model combustor. *Int J Hydrogen Energy* 2020;45:1045–60.
- [41] Huang Z, Zhao M, Zhang H. Modelling n-heptane dilute spray flames in a model supersonic combustor fueled by hydrogen. *Fuel* 2020;264. 116809.
- [42] Zhao M, Li JM, Teo CJ, Khoo BC, Zhang H. Effects of variable total pressures on instability and extinction of rotating detonation combustion. *Flow, Turbul Combust* 2020;104:261–90.
- [43] Li Q, Wang Z. Dynamic mode decomposition of turbulent combustion process in DLR scramjet combustor. *J Aerosp Eng* 2017;30. 04017034–1–10.
- [44] Zhao M, Chen ZX, Zhang H, Swaminathan N. Large eddy simulation of a supersonic lifted hydrogen-air flame with perfectly stirred reactor model. *Proc Combust Inst* 2020.
- [45] Pope SB. Ten questions concerning the large-eddy simulation of turbulent flows. *New J Phys* 2004;6:35.
- [46] Bouheraoua L, Domingo P, Ribert G. Large-eddy simulation of a supersonic lifted jet flame: Analysis of the turbulent flame base. *Combust Flame* 2017;179:199–218.
- [47] Vinuesa JF, Porté-Agel F, Basu S, Stoll R. Subgrid-scale modeling of reacting scalar fluxes in large-eddy simulations of atmospheric boundary layers. *Environ Fluid Mech* 2006;6:115–31.
- [48] Cocks P. Large eddy simulation of supersonic combustion with application to scramjet engines. *Dissertation* 2011:293.
- [49] Duwig C, Nogenmyr KJ, Chan CK, Dunn MJ. Large eddy simulations of a piloted lean premix jet flame using finite-rate chemistry. *Combust Theory Model* 2011;15:537–68.
- [50] Krol MC, Molemaker MJ, Vilà Guerau De Arellano J. Effects of turbulence and heterogeneous emissions on photochemically active species in the convective boundary layer. *J Geophys Res Atmos* 2000;105:6871–84.
- [51] Shanbhogue SJ, Husain S, Lieuwen T. Lean blowoff of bluff body stabilized flames: Scaling and dynamics. *Prog Energy Combust Sci* 2009;35:98–120.
- [52] Segal C. *The scramjet engine: Processes and characteristics*. Cambridge, U.K.: Cambridge University Press; 2009.
- [53] Damköhler G. Influence of diffusion, fluid flow, and heat transport on the yield in chemical reactors. *Int Chem Eng* 1988;28:132–98.
- [54] Kim SO, Luong MB, Chen JH, Yoo CS. A DNS study of the ignition of lean PRF/air mixtures with temperature inhomogeneities under high pressure and intermediate temperature. *Combust Flame* 2015;162:717–26.
- [55] Biswas S, Tanvir S, Wang H, Qiao L. On ignition mechanisms of premixed CH₄/air and H₂/air using a hot turbulent jet generated by pre-chamber combustion. *Appl Therm Eng* 2016;106:925–37.
- [56] Snegirev AY. Perfectly stirred reactor model to evaluate extinction of diffusion flame. *Combust Flame* 2015;162:3622–31.
- [57] Barlow RS, Dibble RW, Chen JY, Lucht RP. Effect of Damköhler number on superequilibrium OH concentration in turbulent nonpremixed jet flames. *Combust Flame* 1990;82:235–51.
- [58] Donbar JM, Gruber MR, Jackson TA, Carter CD, Mathur T. OH planar laser-induced fluorescence imaging in a hydrocarbon-fueled scramjet combustor. *Proc Combust Inst* 2000;28:679–87.
- [59] Richter M, Collin R, Nygren J, Aldén M, Hildingsson L, Johansson B. Studies of the combustion process with simultaneous formaldehyde and OH PLIF in a direct-injected HCCI engine. *JSME Int J, Ser B Fluids Therm Eng* 2006;48:701–7.
- [60] Gordon RL, Masri AR, Mastorakos E. Simultaneous Rayleigh temperature, OH- and CH₂O-LIF imaging of methane jets in a vitiated coflow. *Combust Flame* 2008;155:181–95.
- [61] Yamashita H, Shimada M, Takeno T. A numerical study on flame stability at the transition point of jet diffusion flames. *Symp Combust* 1996;26:27–34.
- [62] Markides CN, Mastorakos E. An experimental study of hydrogen autoignition in a turbulent co-flow of heated air. *Proc Combust Inst* 2005;30:883–91.
- [63] Wang H, Wang Z, Sun M, Qin N. Large eddy simulation of a hydrogen-fueled scramjet combustor with dual cavity. *Acta Astronaut* 2015;108:119–28.
- [64] Demosthenous E, Borghesi G, Mastorakos E, Cant RS. Direct numerical simulations of premixed methane flame initiation by pilot n-heptane spray autoignition. *Combust Flame* 2016;163:122–37.
- [65] Wadekar S, Janas P, Oevermann M. Large-eddy simulation study of combustion cyclic variation in a lean-burn spark ignition engine. *Appl Energy* 2019;255.
- [66] Chen L, Zhang R, Pan J, Wei H. Effects of partitioned fuel distribution on auto-ignition and knocking under spark assisted compression ignition conditions. *Appl Energy* 2020;260.